Ferroelectric ZrO 2 phases from infrared spectroscopy

Ali El Boutaybi, Rebecca Cervasio, Alban Degezelle, Thomas Maroutian, Jean-Blaise Brubach, Valérie Demange, Ludovic Largeau, Marine Verseils, Sylvia Matzen, Guillaume Agnus, et al.

Ferroelectric ZrO 2 phases from infrared spectroscopy

Ali El Boutaybi, Rebecca Cervasio, Alban Degezelle, Thomas Maroutian, Jean-Blaise Brubach, Valérie Demange, Ludovic Largeau, Marine Verseils, Sylvia Matzen, Guillaume Agnus, et al.

Journal of Materials Chemistry C

ROYAL SOCIETY OF CHEMISTRY

PAPER

View Article Online
View Journal

Cite this: DOI: 10.1039/d3tc01985c

Ferroelectric ZrO_2 phases from infrared spectroscopy†

Ali El Boutaybi, *[a] Rebecca Cervasio,[b] Alban Degezelle,[a] Thomas Maroutian,[a] Jean-Blaise Brubach,[b] Valérie Demange,[c] Ludovic Largeau,[a] Marine Verseils,[b] Sylvia Matzen,[a] Guillaume Agnus,[a] Laurent Vivien,[a] Panagiotis Karamanis,[d] Michel Rérat,[d] Pascale Roy[b] and Philippe Lecoeur[a]

Received 8th June 2023,
Accepted 13th July 2023

DOI: 10.1039/d3tc01985c

rsc.li/materials-c

We investigate ferroelectric thin films of ZrO_2 experimentally and theoretically using infrared (IR) absorption spectroscopy coupled with density functional theory (DFT) calculations. The IR absorbance is measured using IR synchrotron radiation, while the theoretical investigations are performed using CRYSTAL suite of quantum chemical programs. Theoretically, we consider the two polar experimentally observed orthorhombic *Pbc*2_1, and rhombohedral *R*3*m* phases, as well as two non-polar phases, tetragonal *P*4_2/*nmc*, and ground state monoclinic *P*2_1/*c*. Experimentally, we follow two approaches to enable IR measurements: (i) direct growth of ZrO_2 films on high-resistive silicon substrates with either a $La_{0.67}Sr_{0.33}MnO_3$ (LSMO) or ZnO buffer layer to induce tensile and compressive strain, respectively, and (ii) transfer of ZrO_2 films, grown initially on LSMO-buffered $SrTiO_3$ or $DyScO_3$ substrates, onto high-resistive silicon substrate as membranes. The far-IR structural signature of the films is assigned to a tetragonal phase, mainly when the film is under tensile strain; however, the ZrO_2 film shows a ferroelectric signature. Under compressive strain, an early stage of phase transition from the non-polar *P*4_2/*nmc* phase to the polar *R*3*m* phase is observed. Our findings open new paths for investigating the origin of ferroelectricity in ZrO_2-based ferroelectric thin films.

1 Introduction

Ferroelectric thin films of HfO_2 and ZrO_2 have recently garnered considerable attention due to their potential applications in various fields such as nonvolatile memories,[1–5] ferroelectric field-effect transistors,[6–8] energy storage,[9–11] negative capacitance,[12–14] and tunnel junctions.[15,16] HfO_2 and ZrO_2 were also considered for nonlinear optical applications, as they are compatible with silicon photonics.[17–20] Indeed, one of the major advantages of these materials is their compatibility with silicon technology, making them highly scalable.[6,21]

As the interest in HfO_2 and ZrO_2-based ferroelectric materials for future applications follows an exponential growth, it is crucial to understand the origin of the ferroelectric phase. Since the discovery of ferroelectricity in HfO_2 in 2011 by Boscke *et al.*,[22] numerous studies have been conducted on such compounds, aiming to improve their ferroelectric properties,[23–25] as well as to gain a fundamental understanding of the origin of ferroelectricity.[26–28] It was first shown that the orthorhombic phase (*Pbc*2_1, No. 29, o phase) is responsible for the ferroelectric behavior observed in Si-doped HfO_2 polycrystalline thin films,[22] then the same phase was reported in a lot of different HfO_2 and ZrO_2-based ferroelectric thin films.[29–33] In addition, a ferroelectric rhombohedral phase (*R*3*m*, No. 160, r phase) has been reported in HfO_2, and ZrO_2-based epitaxial thin films.[34–37] A distorted orthorhombic phase has been reported in Y-doped HfO_2 with improvement in polarization.[38] First-principles calculations have demonstrated other possible ferroelectric phases in HfO_2 and ZrO_2 materials, such as rhombohedral *R*3,[39] orthorhombic *Pmn*2_1,[40,41] and monoclinic *Pc*.[42] In addition to the ferroelectricity in HfO_2 and ZrO_2, antiferroelectricity has also been observed in pure ZrO_2, and ZrO_2-rich thin films.[43–46]

Most studies in the literature on HfO_2 and ZrO_2 ferroelectric thin films use X-ray Diffraction (XRD) for structure determination. However, due to the polymorphism of HfO_2 and ZrO_2, the analysis of their structure using XRD can be challenging. Apart from the two polar phases experimentally reported (o and r phases) and three suggested theoretically (*R*3, *Pmn*2_1, and *Pc* phases), a large variety of other phases composes the phase diagram of ZrO_2 and HfO_2, including the ground state monoclinic phase

[a] Centre de Nanosciences et de Nanotechnologies (C2N), Universite Paris-Saclay, CNRS, Palaiseau, France. E-mail: ali.el-boutaybi@c2n.upsaclay.fr
[b] Synchrotron SOLEIL, L'Orme des Merisiers, 91192 Gif-sur-Yvette Cedex, France
[c] ISCR Univ Rennes, CNRS, ISCR—UMR 6226, ScanMAT—UMS 2001, Rennes, France
[d] Université de Pau et des Pays de l'Adour, CNRS, IPREM, E2S UPPA, Pau, France

† Electronic supplementary information (ESI) available. See DOI: https://doi.org/10.1039/d3tc01985c

($P2_1/c$, No. 14, m phase),[47,48] high temperature tetragonal ($P4_2/nmc$, No. 137, t phase) and cubic ($Fm\bar{3}m$) phases,[49] and high-pressure phases.[50–52] These various phases in HfO_2- and ZrO_2-based materials make their structural characterization challenging.

Recently, Raman and infrared (IR) spectroscopies have been used as alternative methods to characterize these materials and identify their structure.[53–55] Raman and IR reflectance were used to study Y-doped HfO_2 in a bulk-like state,[55] and some characteristic vibrational phonon modes have been identified,[55] also from first-principles calculations.[56] Similarly, Raman was used to investigate the ferroelectricity and antiferroelectricity in polycrystalline Si-doped ZrO_2.[46] However, regarding epitaxial HfO_2 and ZrO_2 thin films, neither Raman nor IR activities were reported so far. Indeed, such systems are challenging for optical spectroscopies because the quantity of matter to probe is small (about 10 nm thickness), and the contribution of the substrate very often masks the ultrathin film signal.

Herein, we investigate the IR absorbance of epitaxial ferroelectric ZrO_2 thin films on a high resistive silicon substrate (Si-HR), either grown directly through the use of buffer layers or transferred as membranes after the epitaxial growth on perovskite oxide substrates. Notice that probing the individual IR signature of the film when deposited directly on these latter substrates would be extremely difficult, due to their strong response in both absorption and reflectance configurations. On the other hand, as the IR beam can be readily transmitted through the Si-HR substrate, hence the IR absorbance of the ZrO_2 thin films can be obtained. For proper assignment of IR bands in our experimental result, we employed first-principles calculations using CRYSTAL code to investigate the IR activities and simulate the IR absorbance of the different phases of ZrO_2.

2 Computational and experimental details

Theoretical investigation

We conducted calculations using the CRYSTAL17 suite of programs, an *ab initio* periodic code based on the atom-centered Gaussian basis set.[57] We employed basis sets taken from ref. 58–60 for O and Zr, respectively, in our calculations for ZrO_2. We utilized the three-parameter, Lee–Yang–Parr exchange–correlation (B3LYP) hybrid functional,[61,62] known to provide accurate vibrational frequencies,[19,63] relying on all-electron density functional theory (DFT) calculations. The calculations were performed using an $8 \times 8 \times 8$ Monkhorst–Pack scheme[64] for the k-point mesh in the Brillouin zone (BZ). To evaluate the precision of the Coulomb and Hartree–Fock exchange series, we used five parameters[65,66] with values of 8, 8, 8, 8, and 16. The self-consistent field energy threshold was set to 10^{-8} Ha for geometry optimization and frequency calculation. Our focus was on comparing the IR absorbance signature of different phases to the experimental IR absorbance measured with IR synchrotron light of ZrO_2 thin films. We simulated the absorbance using CRYSTAL code based on the polarity evaluation of IR modes, which is a fully analytical method for calculating Born charges and infrared intensities of periodic systems.[67] And the calculation of the vibrational modes and their frequencies in our simulations was based on the assumption of harmonic behavior. This approach is well-established and has been implemented in the CRYSTAL code.[68]

Sample fabrication

On the experimental part, we used two approaches to be able to measure ZrO_2 thin films by IR transmission. In the first approach, ZrO_2 films were grown directly on $La_{0.67}Sr_{0.33}MnO_3$ (LSMO)/Perovskite nanosheet-buffered and ZnO/Yttria stabilized zirconia (YSZ)-buffered Si-HR substrates using pulsed laser deposition (PLD) with the same conditions as described in ref. 36. To grow LSMO on Si-HR, nanosheets (NS) of calcium niobate ($Ca_2Nb_3O_{10}$) with a thickness of about 1 nm were first deposited as a template for perovskite oxide growth.[69] The LSMO layer further grown on NS-buffered Si-HR was 18 nm thick, while the thickness of the other ZnO/YSZ buffer was 15 nm. On both these types of buffered Si-HR substrates, the thickness of the ZrO_2 films was 22 nm. Si-HR was chosen because it does not absorb in the IR region, which facilitates IR investigation based on the transmission of the IR beam through the sample. LSMO/NS/Si-HR and ZnO/YSZ/Si-HR samples were used as a reference to obtain the IR absorbance of ZrO_2 thin films.

In the second approach, we investigated ZrO_2 thin films as membranes transferred onto Si-HR substrates. To do so, we grew two 27 nm-thick ZrO_2 films, one on LSMO-buffered (001)-oriented $SrTiO_3$ (STO) and one on (110)-oriented $DyScO_3$ (DSO) substrate using the same conditions as reported in ref. 36. After the growth, the two thin films were released from the substrate by chemically etching the LSMO layer and transferring ZrO_2 membranes onto the Si-HR substrate. Note that releasing a thin film can cause a change of the strain in the film, but it does not necessarily cause a phase transition, as observed in $Hf_{0.5}Zr_{0.5}O_2$ (HZO) thin films.[70]

IR measurements

The ZrO_2 films were measured using the infrared spectroscopy beamline AILES (Advanced Infrared Line Exploited for Spectroscopy), Synchrotron SOLEIL.[71] Exploiting the high brightness of the synchrotron radiation source, far-IR spectra in the 30–700 cm^{-1} range were obtained using a Bruker IFS125HR Fourier transform spectrometer evacuated at pressures lower than 10^{-4} mbar to avoid absorption by water and residual gas. A spectral resolution of 2 cm^{-1} was chosen. A 6 microns Mylar beamsplitter combined with a bolometer cooled at 4.2 K completes the setup.

3 Results and discussion

3.1 Theoretical IR active phonon modes

Non-polar ZrO_2 phases. First, the ground state $P2_1/c$ m phase and the $P4_2/nmc$ t phase, known to be stable when the grain size

or film thickness is below 30 nm,[26,72] have been considered for the theoretical investigation. For the latter, a unit cell containing 6 atoms for IR investigations was used, which resulted in 18 vibrational modes: 3 for translation and 15 for optical phonon modes. The t phase displays only three distinctive IR fingerprints at 138, 333, and 426 cm^{-1}, all active in experimental IR (Fig. 1b). The peak positions are indicated by bars in Fig. 1b. The phonon frequencies of IR active modes obtained using B3LYP functional agree with earlier experimental measurements performed by Bonera *et al.* who reported three peaks for ZrO_2 t phase at 150, 338 and 430 cm^{-1}.[73] The simulated IR absorbance for the t phase, as shown in Fig. 1b, indicates three different bands; the two bands at low energy have almost similar intensities, while the band around 426 cm^{-1} exhibits much stronger intensity in good agreement with previous calculations.[26] Regarding the ground state m phase, a unit cell containing 12 atoms was used, resulting in 36 vibrational modes: 3 for translation modes and 33 for optical phonon modes. The m phase presents richer IR active modes (15 active IR modes), resulting in 9 bands in the simulated IR absorbance spectra of Fig. 1a.

Polar ZrO_2 phases. For the two experimentally reported polar phases, o and r phases, a unit cell with 12 atoms was used to investigate the IR absorbance. The o phase exhibits 24 out of 33 optical modes being active in IR. As shown in Fig. 1c, the simulated IR absorbance for the o phase reveals a much richer pattern compared to the t phase, with at least 8 bands being observed, four of which having high intensity. Among these bands, the one located at around 400 cm^{-1} resulting from B_2 and B_1 modes is found only in the o phase and can serve as a strong signature of this phase. This was also identified as an IR fingerprint for o HfO_2.[55] In addition, three bands of almost equal intensity located at 228, 329, and 445 cm^{-1} can also help in identifying the o phase of ZrO_2.

On the other hand, in the r phase, from 33 optical phonon modes, 19 modes are IR active and contribute to the IR response. However, during the simulation of IR absorbance of the r phase, only 9 modes exhibited high intensity (> 80 km mol^{-1}), resulting in five IR absorbance bands (Fig. 1d). Of these bands, three are nearly equal in intensity and are located at around 230, 350, and 455 cm^{-1}, while the other two bands at 533 and 680 cm^{-1} are less intense. The IR pattern of the r phase is quite similar to that of the t phase, particularly the two bands at 350 and 455 cm^{-1}, with the main difference being a slight shift to higher energy and similar intensity for these two bands in the r phase. The band that differs the most from the t phase is the one located at 230 cm^{-1}. It should be noted that the IR absorbance given for the r phase was computed at the experimental volume to obtain only real phonon frequencies, with pressure applied to the unit cell, as this phase is unstable at the optimized volume[19] (see also Fig. S2, ESI†). It is also important to note that other factors, such as oxygen vacancies, elastic interaction with the substrate, a specific orientation of the thin film, *etc.*, may stabilize the r phase, which are not considered in this study.

For a comprehensive list of all IR active modes and their corresponding intensities for the investigated phases, refer to Tables S1 and S2 in the ESI.† Additionally, as mentioned in the introduction, first-principles calculations suggest the stability of other polar phases, including the *Pc* and $Pmn2_1$ phases. Although these phases have not been observed experimentally yet, the *Pc* phase was found to have low bulk energy, similar to the o phase in HfO_2 and ZrO_2,[42] while the $Pmn2_1$ phase was found to have lower energy than the t phase in HfO_2,[41,42] and higher energy in ZrO_2.[42] The IR active phonon modes of these two phases were also calculated and are given in the ESI.†

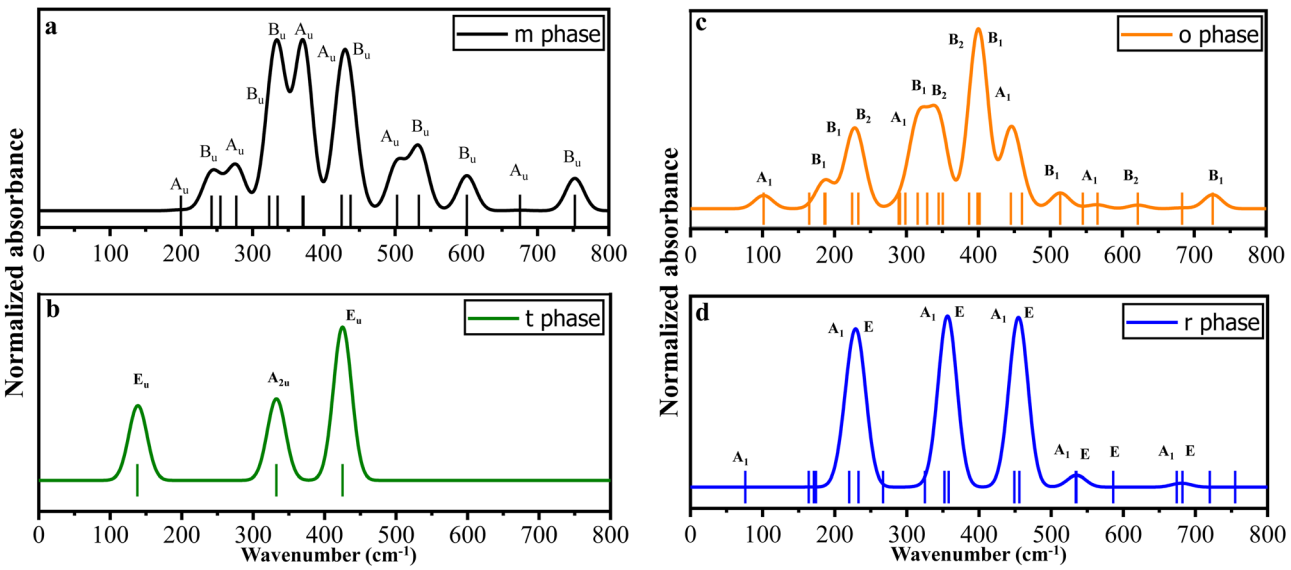

Fig. 1 Infrared absorbance responses of ZrO_2 in different phases, including the non-polar m (a) and t (b) phases and the polar o (c) and r (d) phases. All IR active modes are highlighted in bar form, with emphasis on the modes contributing most to IR absorbance (> 80 km mol^{-1}, see Table S1, ESI†). For exact phonon frequencies and intensities, see Tables S1 and S2 in the ESI.†

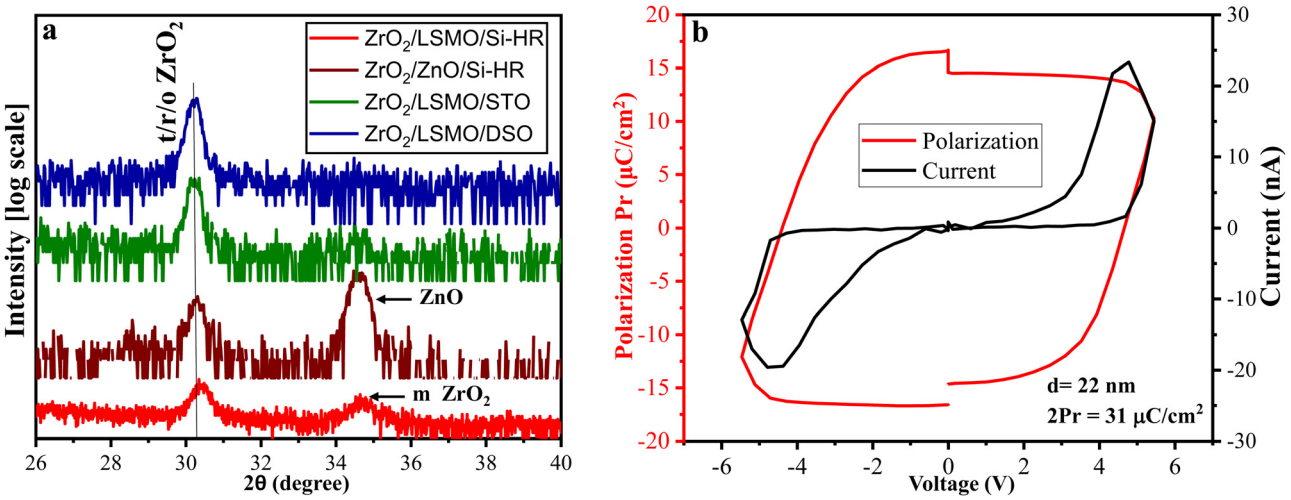

Fig. 2 XRD and *P*–*E* Results: (a) out-of-plane θ–2θ scans for ZrO_2 thin films on LSMO-buffered STO, DSO, and Si-HR substrates, as well as on a Si-HR substrate with a ZnO-YSZ buffer layer. (b) Hysteresis loop of the ferroelectric polarization of the ZrO_2 thin film on LSMO-buffered Si-HR substrate and its corresponding current switching loop (PUND technique).

The simulated IR absorbance of ZrO_2 thin films reveals distinct differences between polar and non-polar phases, in contrast to XRD where most phases, especially the polar ones (Fig. 2), exhibit diffraction peaks at around 30° in out-of-plane θ–2θ scans. These insights can be utilized as a means to distinguish and identify the phases in ZrO_2 thin films.

3.2 Epitaxial ferroelectric ZrO_2 thin films

X-ray diffraction and in-plane strain. As shown in Fig. 2a, the out-of-plane θ–2θ scans for ZrO_2 on ZnO-YSZ and LSMO buffered NS/Si-HR, STO, and DSO substrates are displayed. Each peak is labeled to indicate its corresponding crystal phase, but the most important peak is around 30°, corresponding to the (111)-oriented ZrO_2 thin films. On STO and DSO substrates, this peak is located at around 30.20°, and generally, the films grown on these substrates are under compressive strain.[34,36] This is also the case when using ZnO as a template (Fig. 2a). Conversely, on the LSMO-buffered Si-HR substrate, the ZrO_2 peak is observed at a value of 30.40°, which indicates that the film is under tensile strain. Here, it is worth noting that experimentally and theoretically, the growth of the orthorhombic phase was found to be favored under tensile strain.[23,74–76] Also, on the LSMO-buffered Si-HR substrate, a peak around 34.3° is observed for this 22 nm-thick ZrO_2 film, which can be ascribed to the ground state m phase. This peak was found to appear only at thicknesses above 37 nm for ZrO_2 grown on DSO substrate.[36] The presence of the m phase at a lower thickness here might be due to the NS seed layer, which affects both the LSMO bottom electrode and the strain in the ZrO_2 film (tensile on NS/Si-HR *vs.* compressive on DSO or STO).

Ferroelectric polarization. For electrical characterization, a ferroelectric tester (AiXACCT, TF analyzer 1000) was used on Pt/ZrO_2/LSMO capacitors. The ferroelectric response was obtained through Positive Up Negative Down (PUND) measurements. This measurement was conducted in particular to verify the ferroelectric properties of the ZrO_2 thin film grown on LSMO/NS/Si-HR. The measured hysteresis loop is shown in Fig. 2b, and clear ferroelectric behavior is observed, with a polarization of about 15 μC cm^{-1}. However, we could not perform this measurement on ZnO-YSZ/Si-HR, as the ZnO-YSZ buffer is dielectric. The ferroelectricity of ZrO_2 thin films on STO and DSO substrates has already been reported elsewhere, with a polarization of about 20 μC cm^{-1} for the same thickness range.[36,77] It is worth noting that the higher polarization observed in ZrO_2 on STO and DSO substrates could be attributed to the presence of compressive strain, which enhances the polarization effect.[34,35]

IR absorbance of ZrO_2 on buffered Si-HR. The experimental IR absorbance of the ZrO_2/LSMO/NS/Si-HR sample is presented in Fig. 3a, with three prominent peaks observed at 139, 335, and 432 cm^{-1}, in close agreement with the theoretical values and intensities, corresponding to the t phase (indicated in black bars in Fig. 3a). However, four additional peaks with much lower intensity are also observed, which might be due to the presence of the m phase as observed by XRD in Fig. 2a. The peaks at 514 and 566 cm^{-1} are more likely to correspond to the ground state of ZrO_2 (see Fig. 1a). From the simulated IR in Fig. 1a, the m phase displays an IR band at around 515 cm^{-1} with two peaks at 505 and 532 cm^{-1} (corresponding to A_u and B_u modes). Note that the o and r phases also display a band around 530 cm^{-1}, and distinguishing these phases based only on this low-intensity band is difficult. The two bands located at 75 and 261 cm^{-1} are very low in intensity and can be caused by the strain from the substrate on the ZrO_2 thin film. Nevertheless, Fig. 3a demonstrates a clear signature of the t phase.

The ZrO_2 thin film on LSMO/NS/Si-HR is under tensile strain, as indicated by the shift of the (111) peak to a higher 2θ value (30.40°, Fig. 2a). This suggests that the film may adopt the o phase, as reported in previous studies on HfO_2-based ferroelectric thin films.[23,74–76] However, from the IR spectra,

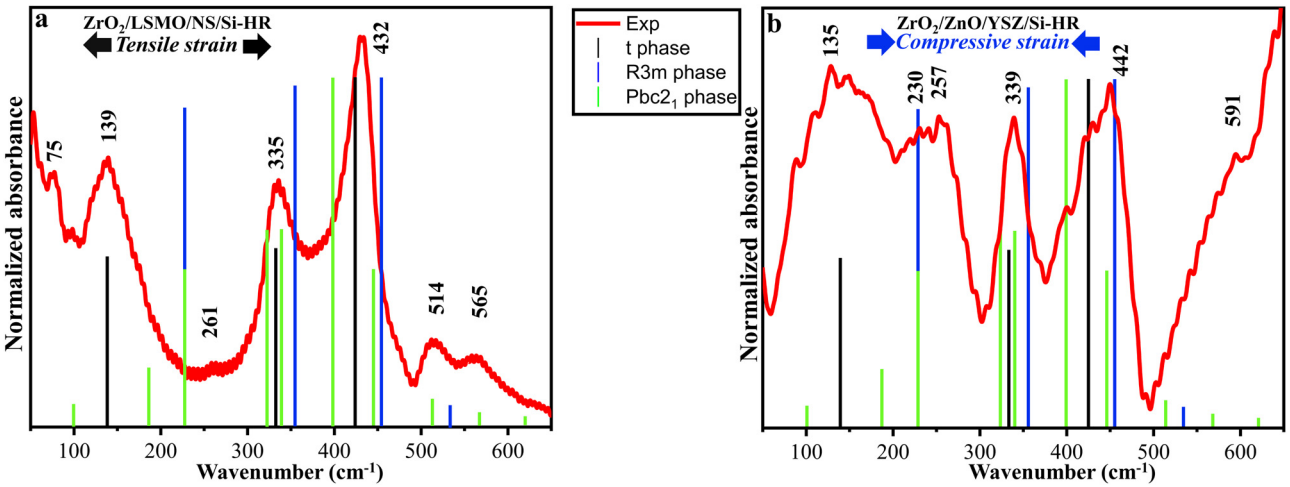

Fig. 3 Infrared absorbance responses on Si-HR: (a) and (b) show the experimental IR absorbance spectra (in red color) of ZrO_2 thin films grown on LSMO- and ZnO-YSZ-buffered Si-HR substrates, respectively. The IR absorbance spectra obtained using the CRYSTAL code are also provided for t, o, and r phases presented in bar form, based on the intensity of each mode, as shown in Fig. 1.

the tensile strain on the ZrO_2 thin film does not appear to be sufficient to induce a phase transition from the t to the polar o phase. Also, the main intense and characteristic IR absorbance band at around 400 cm^{-1} of the o phase (also common with the *Pc* phase see Table S1, ESI†) as shown in Fig. 1c is not observed. On the other hand, the hysteresis loop (Fig. 2b) clearly indicates that the ZrO_2 thin film displays ferroelectric behavior. At the same time, none of the four considered polar phases (o, r, *Pc*, and $Pmn2_1$) were detected in the IR absorbance. Therefore, the origin of the observed ferroelectric behavior has to be found elsewhere, such as in the breaking of the t phase symmetry or in a new polar phase with close symmetry to the tetragonal one. Also, oxygen vacancy migration might contribute to such response.[78]

It is worth noting that tetragonal ZrO_2 was found to exhibit antiferroelectric behavior,[43] which was later explained by a transition from the non-polar t phase to the polar o phase.[79] However, despite a clear t phase signature of our ZrO_2 thin films, no antiferroelectric double hysteresis loop of the polarization was observed. This underlines the need for further experimental and theoretical studies to understand the origin of both ferroelectric and antiferroelectric behaviors in ZrO_2 thin films.

The ZrO_2 thin film grown on ZnO-YSZ/Si-HR is found to be under compressive strain, comparable to the one in ZrO_2 films obtained on STO and DSO substrates (see Fig. 2a). The experimental IR absorbance spectrum is presented in Fig. 3b. The simulated IR absorbance positions of t, r, and o phases are also indicated. Three IR absorbance bands corresponding to the t phase are observed, but with decreased intensity, especially for the band at around 426 cm^{-1} (E_u mode), which was found to have the highest intensity by DFT and confirmed by experiment (Fig. 3). On ZnO-YSZ/Si-HR, its intensity is equivalent to the other two bands at 130 and 339 cm^{-1}. This decrease in intensity should thus be attributed to the compressive strain induced by the substrate and buffer layers on the ZrO_2 thin film. A shift of the IR bands to higher energy is also observed, indicating a possible phase transition from the t phase to the r phase under compressive strain, as the simulated IR absorbance of the r phase (Fig. 1d) is close to the experimental one given in Fig. 3b. Note that a highly compressed r phase was obtained in an HZO thin film grown on a ZnO substrate.[37] However, in our case, the compressive strain seems lower and close to the one induced by STO and DSO substrates (Fig. 2a). This is because ZrO_2 has higher lattice parameters compared to HZO and HfO_2, and the 10 nm ZnO thin film used here as a template might not have exactly the same lattice parameters as the bulk ZnO substrate.

In addition to the changes observed in the intensity and position of the IR absorbance bands corresponding to the t phase, Fig. 3b also reveals a new absorbance band at around 230–257 cm^{-1}. This band has comparable intensity to the bands at 339 cm^{-1} and 442 cm^{-1}. This is likely associated with the r phase, as these results are consistent with DFT calculations presented in Fig. 1d, where three IR absorbance bands are found at 230, 350, and 450 cm^{-1}. These findings suggest that the t phase is more likely to transform to the rhombohedral phase when a ZrO_2 thin film is under compressive strain, confirming the impact of compressive strain on r phase stability, as previously reported in the literature.[34–37] However, a signature of the t phase is still detectable (band around 135 cm^{-1}), indicating that it is still present and not completely transformed to the r phase.

IR absorbance of ZrO_2 membranes. ZrO_2 membranes were used as it was not possible to perform the same measurement as on Si-HR substrate on perovskite substrates (STO and DSO). Indeed, these two substrates are interesting because they have been found to stabilize the r phase,[34–36] and also the orthorhombic o and rhombohedral-distorted o phases.[30,38] IR spectroscopy can help to identify crystal phonon activities and hence distinguish these different polymorphs of ZrO_2 and HfO_2. On the other hand, direct IR measurement is challenging as perovskite substrates are thick for IR reflectance and not

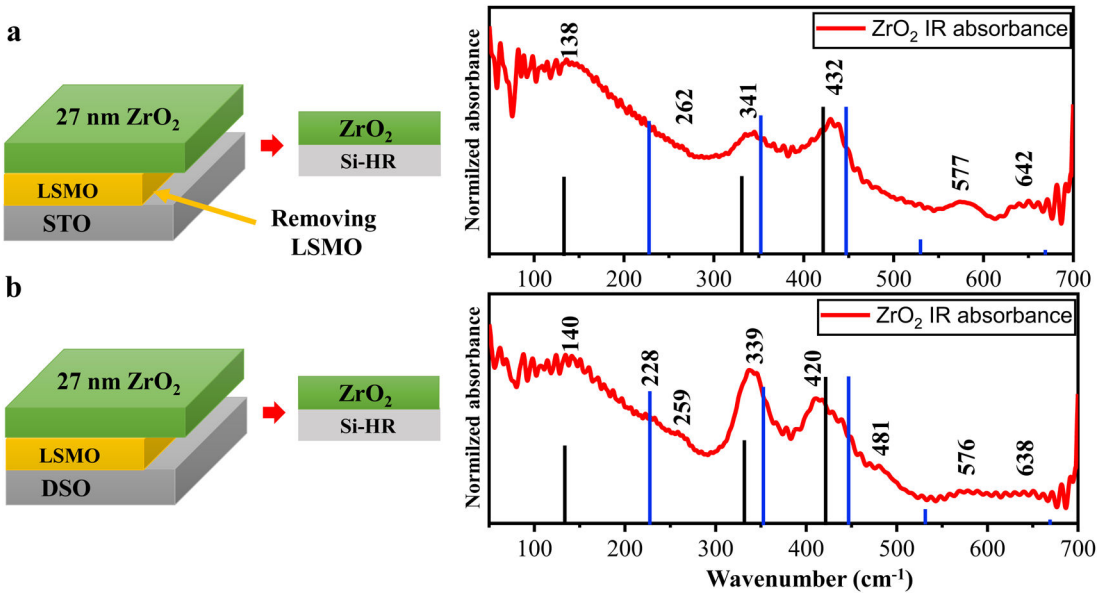

Fig. 4 Infrared absorbance responses of ZrO_2 membranes on Si-HR: (a) and (b) show IR absorbance of ZrO_2 membranes, which were initially grown on LSMO-buffered STO and DSO substrates, respectively, and then transferred onto the Si-HR substrate for IR measurements.

transparent for IR transmission. Thus, using ZrO_2 membranes can be useful to access crystal symmetry, even though releasing a ZrO_2 film might change the strain applied to it. Note that HZO membranes have already been studied, and it was found that releasing a membrane affects the rhombohedral distortion while the film remains ferroelectric.[37] Therefore, releasing a thin ZrO_2 film might change the strain applied to the film, but it should not affect the initial growth phase symmetry.

Fig. 4a and b display the experimental IR absorbance for two ZrO_2 membranes released from STO and DSO substrates, respectively. At first glance, three peaks characterizing the t phase are observed, but with different intensities from the ones reported in Fig. 3. Also, the two bands at around 340 and 430 cm^{-1} display the same intensity as when the film was under a compressive strain (Fig. 3b). This indicates that the compressive strain has more effect on ZrO_2 t phase signature than the tensile strain as far as IR absorbance is concerned, with IR bands closer to the ones of the r phase. This can be seen as compressive strain favoring the r phase, in good agreement with previous reports.[34–37]

Furthermore, the positions of these peaks are generally affected by ± 10 cm^{-1}, which can be due to strain caused by the substrate, but also to the strain caused by the release of the ZrO_2 films. In addition, other bands are observed for ZrO_2 released from STO and DSO substrates. ZrO_2 membrane released from the DSO substrate differs from STO in 2 bands at around 228 and 481 cm^{-1}: the band at 228 cm^{-1} is not observed in Fig. 4a, as it might be covered by the large band between 138 and 262 cm^{-1}; while for the band at 481 cm^{-1}, it could be caused by the anisotropy of the DSO substrate, resulting in a different distortion of ZrO_2 thin film compared to STO substrate.

Although there may be slight variations between the films grown on STO and DSO substrates, their IR spectra are remarkably similar, suggesting that they correspond to the same initial phase developed on these substrates. This can be observed by examining the three bands of the t phase, as well as the two new bands at higher energies (above 500 cm^{-1}), which are detected at the same positions in both films. These higher energy bands cannot be observed on ZrO_2 film on ZnO-YSZ-buffered Si-HR (Fig. 3b) due to the large absorption of ZnO at higher energy.[80,81]

Strain effect on IR phonon modes. As depicted in Fig. 2, the films are subjected to different strains, which have the potential to disrupt the symmetry of the t or *R3m* phase. This symmetry-breaking effect results in the activation of additional IR-active modes. Specifically, focusing on the t phase, we found that the removal of symmetry alone does activate additional IR modes, although their intensity is negligible (Fig. S3, ESI†). However, the introduction of strain, such as through tensile strain, causes a shift of the IR bands towards higher energy (Fig. S4, ESI†), particularly the lower IR bands, which are more sensitive to strain compared to the higher bands. This effect is also observed when applying compressive strain (see Fig. S4 and S5, ESI†). Additionally, the application of a compressive strain on t and *R3m* phases is found to amplify the additional IR bands (at 544 and 655 cm^{-1}) to greater intensities than with tensile strain (Fig. S4 and S5, ESI†), in good agreement with the experimental results (Fig. 4).

3.3 Tetragonal *vs.* rhombohedral phases

As mentioned above ZrO_2 film on ZnO-YSZ/Si-HR experiences compressive strain, which stabilizes the r phase, as reported in previous studies.[34–37] The experimental IR absorbance of the film reveals three bands of comparable intensity and proximity to the simulated IR of the r phase. Based on this observation, we aim to investigate the possibility of a phase transition from

t to r phase, which has not yet been explored in the literature. To achieve this, we examined the instability observed at the Γ point in the r phase. Specifically, this involved following the unstable E phonon mode by displacing the atoms around their original positions and evaluating the energy landscape at each step to identify the lowest energy minima (Fig. 5a). The energy scan revealed two additional lower energy phases, labeled as w_1 and w_2, with w_2 being energetically closer to the r phase. The re-optimized structure obtained at w_1 (Fig. 5b) corresponds to a new monoclinic phase identified as *Cm* (No. 8). Upon careful analysis, it is revealed that this *Cm* phase is essentially a distorted version of the t phase, with slight distortion in the unit cell angle (Fig. 6 and Table S4, ESI†). Importantly, there is negligible energy difference between these two phases (less than 0.001 meV), and their IR absorbance spectra also show no significant difference (Fig. S6, ESI†). The distinction lies primarily in their structural representation: the t phase can be described using 6 atoms (Fig. 6a), while the *Cm* phase requires 24 atoms and exhibits a small deviation from the symmetrical unit cell angle, disrupting the symmetry of the t phase (Fig. 6b).

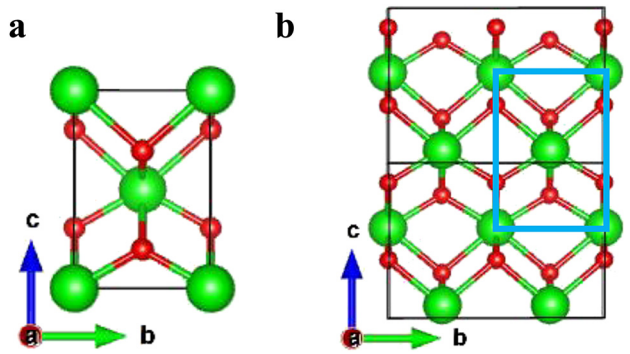

Fig. 6 (a) Tetragonal phase of ZrO_2. (b) *Cm* phase of ZrO_2 with two unit cells (the lattice parameters and the atomic positions are given in Table S4, ESI†).

Another key difference arises from this symmetry disruption: the t phase is non-polar, whereas the *Cm* phase exhibits polarity. However, the polarization of the *Cm* phase was evaluated using the Berry phase method and found to be 0.08 μC cm^2,

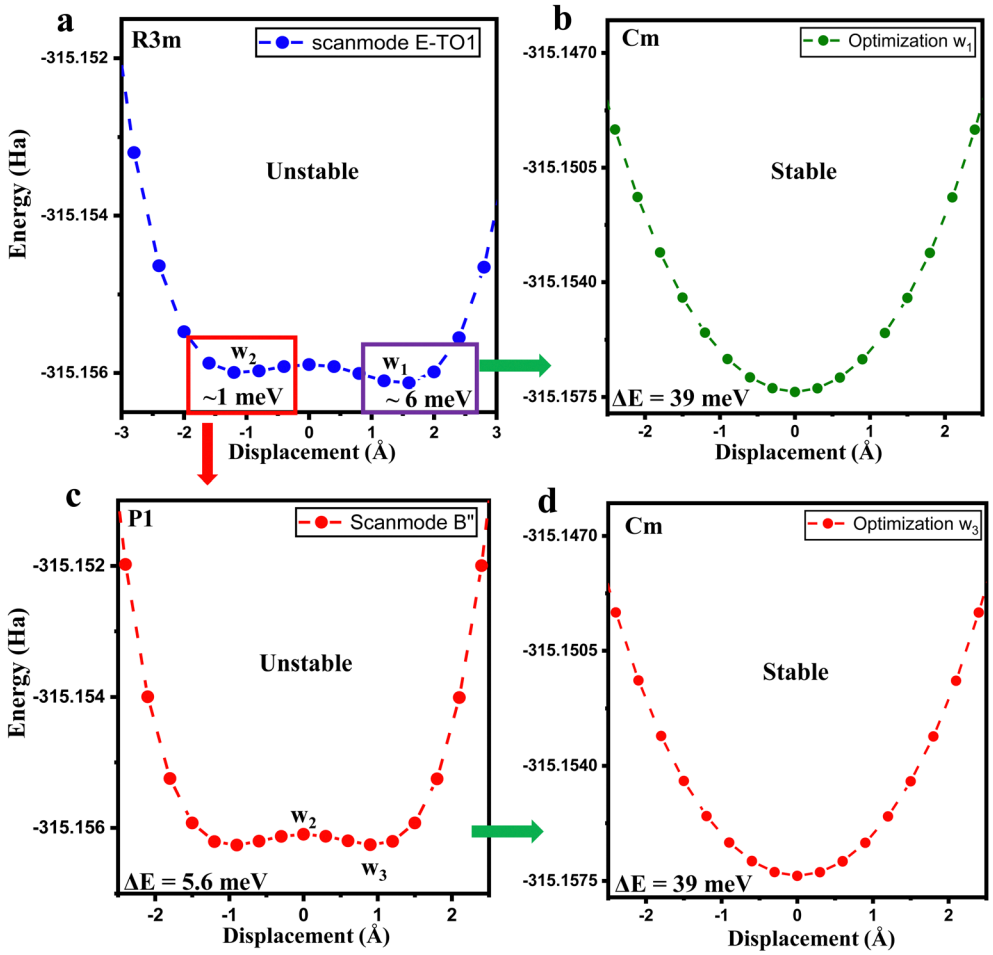

Fig. 5 (a) Energy scanning along the normal mode E (TO1) for the r phase. (b and d) Depict the energy landscapes of the phases obtained at w_1 and w_3 after geometry re-optimization, while (c) shows the energy scan along the unstable B″ mode of the *P*1 phase. The energy indicated in (a) corresponds to the energy difference between the r phase and the two lowest minima prior to re-optimization. In (b)–(d), ΔE is given for the energy minima with respect to the r phase.

a very low value, which is of the same order as the one calculated for the unstrained *R*3*m* phase.[34] The energy difference (ΔE) between the t phase (or *Cm* phase) and the r phase is approximately 39 meV (Fig. 5), which aligns with previous calculations.[36]

On the other hand, the energy minimum at w_2 corresponds to an intermediate phase with space group *P*1, which is identified as unstable (Fig. 5c and Table S3, ESI†). By tracking the unstable B″ mode at the Γ point, two symmetric and similar regions with minimum energy, labeled as w_3, were identified. These minima once again correspond to the aforementioned *Cm* phase (Fig. 5d). These findings suggest the existence of two possible pathways for transitioning from the *Cm* (or distorted t) phase to the r phase: a direct path from *Cm* to r and an indirect path from *Cm* to *P*1, and subsequently to the r phase.

It is important to highlight that the transition from the r phase to the *Cm* phase, as discussed above, cannot be considered purely displacive in nature. This is evident from the fact that the adjustment of atomic positions around the unstable mode breaks the 3-fold axis of the r phase. Similarly, the transition from a 3-fold (*R*3*m*) to a 4-fold ($P4_2/nmc$) symmetry cannot be attributed solely to one phonon mode; it likely involves a combination of multiple phonon modes.[82] However, in the case of thin films, various factors, including compressive strain as depicted in Fig. 2a, as well as surface effects, have been shown to influence the stability of the *R*3*m* phase.[34,36] These factors could generate additional stress on the ZrO_2 film, potentially contributing to the stabilization of the r phase.

Furthermore, the literature suggests that the formation of the rhombohedral phase in fluorite oxides is often associated with ordered oxygen vacancies along the [111] direction of the rhombohedral lattice.[83–85] However, in the case of ZrO_2, the mechanism underlying the formation of the rhombohedral phase is not yet fully understood or extensively studied. Most research has focused on partially stabilized ZrO_2, where the transition occurs from the cubic to rhombohedral phase.[86,87] In certain cases, irradiation of cubic yttria-stabilized zirconia with He ions can induce a cubic-to-rhombohedral phase transformation, leading to a rhombohedral deformation of the cubic cell along the [111] direction due to residual stresses induced by implantation.[88] Although a few studies have reported the transformation from the t to the rhombohedral phase,[89–91] further research is required to fully elucidate the mechanism of this transformation in ZrO_2.

Taking into consideration the fact that the stable phase of ZrO_2 at reduced thickness is tetragonal, the application of epitaxial strain can break the symmetry of the t phase. This allows for the possibility of stabilizing the distorted t phase (*Cm*) and transforming it into the r phase under compressive strain (Fig. 3b), as observed in Fig. 5. The energy cost associated with this phase transition is approximately 9.75 meV per f.u. It should be noted that when considering the instability of the *R*3*m* phase, the optimized volume was used (Fig. 5), while when evaluating the IR absorbance of the r phase, the experimental volume was used as explained earlier (Fig. 1 and Fig. S2, ESI†). This distorted t to r phase transition might offer a new path to investigate the high polarization reported experimentally in the r phase, which is in discrepancy with DFT predictions of low polarization.[34,92] However, other factors, such as oxygen vacancies and the interaction between the ZrO_2 film and the substrate, may also contribute to stabilizing the rhombohedral phase.

4 Conclusion

In this study, we investigated ZrO_2 phases using a combination of first-principles calculations and experimental characterizations. First, we employed the CRYSTAL package to examine the IR activities of ZrO_2 in various phases and simulate its IR absorbance. Then, we performed IR absorbance measurements using two approaches: direct characterization of ZrO_2 thin films grown on a Si-HR substrate and transfer of ZrO_2 films grown on perovskite substrates onto Si-HR for IR characterization. We evidenced that ZrO_2 thin films grown on Si-HR under tensile strain using a LSMO buffer layer exhibit a clear signature of the t phase. Also, we found that ZrO_2 films under in-plane compressive strain with a ZnO-YSZ buffer layer still have a t phase signature in their IR absorbance, but closer to the one of the r phase. This hints at a phase transition from the t phase to the r phase, promoted by the compressive strain. Moreover, the IR absorbance responses of ZrO_2 membranes released from STO and DSO substrate were similar, indicating the same initial phase grown on both substrates, which both induced a compressive strain. Their IR response was also similar to that obtained on ZnO-YSZ-buffered Si-HR substrate. These results suggest that the stable phase of ZrO_2 is tetragonal, and when subjected to compressive strain, it undergoes a phase transition to the rhombohedral phase. On the other hand, the tensile strain does not affect the stability of the tetragonal phase. Surprisingly, despite being a non-polar phase, the film exhibited ferroelectric behavior. This intriguing observation raises questions about the origin of ferroelectricity in the tetragonal phase of ZrO_2. Our findings offer a new direction for investigating the origin of ferroelectricity and high polarization in ZrO_2 and ZrO_2-based ferroelectric thin films by exploring additional factors that may contribute to the observed ferroelectric behavior and also by looking at the transition from t to r phase, rather than solely at the r phase with oxygen vacancies or high compressive strain as in previous studies.

Author contributions

P. L. and T. M. supervised the project and secured the funding together with L. V. A. E. B. prepared all samples, with the help of A. D. for membranes and V. D. and G. A. for NS-buffered Si, and of S. M. for capacitor devices. Structural characterizations were done by A. E. B. and L. L., and ferroelectric measurements by A. E. B. with the help from S. M. R. C. and J.-B. B. did the IR absorbance measurements with help from M. V. and P. R. A. E. B. did the IR data analysis with the help from R. C. A. E. B. did all the *ab initio* calculations, with the help of P. K. and M. R. A. E. B.

wrote the manuscript with the help of T. M. and feedback from all of the authors.

Conflicts of interest

There are no conflicts to declare.

Acknowledgements

This work has received support from the Agence Nationale de la Recherche (ANR) under projects FOIST (N-18-CE24-0030) and FLEXO (N-21-CE09-0046), and from the French national network RENATECH for nanofabrication. Part of this work was granted access to the HPC resources of [CCRT/CINES/IDRIS] under the allocation 2021-2022 [AD010807031R1] made by GENCI (Grand Equipement National de Calcul Intensif). We also acknowledge the ''Direction du Numérique'' of the ''Université de Pau et des Pays de l'Adour'' and the mésocentre Aquitain (MCIA) for their computing facilities. The authors thank G. Baldinozzi (CentraleSupélec, Palaiseau, France) for valuable discussions on the phase transition in ZrO_2.

Notes and references

1 J. Müller, T. S. Böscke, D. Bräuhaus, U. Schröder, U. Böttger, J. Sundqvist, P. Kücher, T. Mikolajick and L. Frey, *Appl. Phys. Lett.*, 2011, **99**, 112901.
2 C. Giovinazzo, J. Sandrini, E. Shahrabi, O. T. Celik, Y. Leblebici and C. Ricciardi, *ACS Appl. Electron. Mater.*, 2019, **1**, 900–909.
3 T. Schenk and S. Mueller, *2021 IEEE International Symposium on Applications of Ferroelectrics (ISAF)*, 2021, pp. 1–11.
4 J. Liao, S. Dai, R.-C. Peng, J. Yang, B. Zeng, M. Liao and Y. Zhou, *Fundam. Res.*, 2023.
5 X. Liu, X. Geng, H. Liu, M. Shao, R. Zhao, Y. Yang and T.-L. Ren, *Tsinghua Sci. Technol.*, 2023, **28**, 221–229.
6 T. Ali, P. Polakowski, S. Riedel, T. Büttner, T. Kämpfe, M. Rudolph, B. Pätzold, K. Seidel, D. Löhr, R. Hoffmann, M. Czernohorsky, K. Kühnel, X. Thrun, N. Hanisch, P. Steinke, J. Calvo and J. Müller, *Appl. Phys. Lett.*, 2018, **112**, 222903.
7 H. Mulaosmanovic, E. T. Breyer, S. Dünkel, S. Beyer, T. Mikolajick and S. Slesazeck, *Nanotechnology*, 2021, **32**, 502002.
8 P. Pujar, H. Cho and S. Kim, *ACS Appl. Electron. Mater.*, 2023, **5**, 11–20.
9 M. H. Park, H. J. Kim, Y. J. Kim, T. Moon, K. D. Kim and C. S. Hwang, *Adv. Energy Mater.*, 2014, **4**, 1400610.
10 M. Hoffmann, U. Schroeder, C. Künneth, A. Kersch, S. Starschich, U. Böttger and T. Mikolajick, *Nano Energy*, 2015, **18**, 154–164.
11 J. P. B. Silva, K. C. Sekhar, H. Pan, J. L. MacManus-Driscoll and M. Pereira, *ACS Energy Lett.*, 2021, **6**, 2208.
12 M. Hoffmann, M. Pešic, K. Chatterjee, A. I. Khan, S. Salahuddin, S. Slesazeck, U. Schroeder and T. Mikolajick, *Adv. Funct. Mater.*, 2016, **26**, 8643.
13 S. Park, M. C. Chun, S. Park, G. yeon Park, M. Jung, Y. Noh, S.-E. Ahn and B. S. Kang, *Curr. Appl. Phys.*, 2019, **19**, 347–350.
14 C.-H. Cheng, C.-C. Fan, C.-Y. Tu, H.-H. Hsu and C.-Y. Chang, *IEEE Trans. Electron Devices*, 2019, **66**, 825–828.
15 Y. Wei, S. Matzen, T. Maroutian, G. Agnus, M. Salverda, P. Nukala, Q. Chen, J. Ye, P. Lecoeur and B. Noheda, *Phys. Rev. Appl.*, 2019, **12**, 031001.
16 S. S. Cheema, N. Shanker, C.-H. Hsu, A. Datar, J. Bae, D. Kwon and S. Salahuddin, *Adv. Electron. Mater.*, 2022, **8**, 2100499.
17 S. Kondo, R. Shimura, T. Teranishi, A. Kishimoto, T. Nagasaki, H. Funakubo and T. Yamada, *Jpn. J. Appl. Phys.*, 2021, **60**, 070905.
18 S. Kondo, R. Shimura, T. Teranishi, A. Kishimoto, T. Nagasaki, H. Funakubo and T. Yamada, *Jpn. J. Appl. Phys.*, 2021, **60**, SFFB13.
19 A. El Boutaybi, P. Karamanis, T. Maroutian, S. Matzen, L. Vivien, P. Lecoeur and M. Rérat, *Phys. Rev. B*, 2023, **107**, 045140.
20 A. E. Boutaybi, T. Maroutian, S. Matzen, L. Vivien, P. Karamanis, M. Rérat and P. Lecoeur, *Oxide-based Materials and Devices XIV*, 2023, p. 124220U.
21 J. Müller, T. S. Böscke, S. Müller, E. Yurchuk, P. Polakowski, J. Paul, D. Martin, T. Schenk, K. Khullar, A. Kersch, W. Weinreich, S. Riedel, K. Seidel, A. Kumar, T. M. Arruda, S. V. Kalinin, T. Schlösser, R. Boschke, R. van Bentum, U. Schröder and T. Mikolajick, *2013 IEEE International Electron Devices Meeting*, 2013, pp. 10.8.1–10.8.4.
22 T. S. Böscke, J. Müller, D. Bräuhaus, U. Schröder and U. Böttger, *Appl. Phys. Lett.*, 2011, **99**, 102903.
23 P. Fan, Y. K. Zhang, Q. Yang, J. Jiang, L. M. Jiang, M. Liao and Y. C. Zhou, *J. Phys. Chem. C*, 2019, **123**, 21743–21750.
24 S. Kang, W.-S. Jang, A. N. Morozovska, O. Kwon, Y. Jin, Y.-H. Kim, H. Bae, C. Wang, S.-H. Yang, A. Belianinov, S. Randolph, E. A. Eliseev, L. Collins, Y. Park, S. Jo, M.-H. Jung, K.-J. Go, H. W. Cho, S.-Y. Choi, J. H. Jang, S. Kim, H. Y. Jeong, J. Lee, O. S. Ovchinnikova, J. Heo, S. V. Kalinin, Y.-M. Kim and Y. Kim, *Science*, 2022, **376**, 731–738.
25 Y. Choi, H. Park, C. Han, J. Min and C. Shin, *Sci. Rep.*, 2022, **12**, 16750.
26 R. Materlik, C. Kunneth and A. Kersch, *J. Appl. Phys.*, 2015, **117**, 10897550.
27 X. Sang, E. D. Grimley, T. Schenk, U. Schroeder and J. A. M. LeBeau, *Appl. Phys. Lett.*, 2015, **106**, 162905.
28 H.-J. Lee, M. Lee, K. Lee, J. Jo, H. Yang, Y. Kim, S. C. Chae, U. Waghmare and J. H. Lee, *Science*, 2020, **369**, 1343–1347.
29 M. H. Park, T. Schenk, C. M. Fancher, E. D. Grimley, C. Zhou, C. Richter, J. M. LeBeau, J. L. Jones, T. Mikolajick and U. Schroeder, *J. Mater. Chem. C*, 2017, **5**, 4677–4690.
30 J. Lyu, I. Fina, R. Solanas, J. Fontcuberta and F. Sánchez, *ACS Appl. Electron. Mater.*, 2019, **1**, 220–228.
31 Q. Luo, Y. Cheng, J. Yang, R. Cao, H. Ma, Y. Yang, R. Huang, W. Wei, Y. Zheng, T. Gong, J. Yu, X. Xu, P. Yuan, X. Li, L. Tai,

H. Yu, D. Shang, Q. Liu, B. Yu, Q. Ren, H. Lv and M. Liu, *Nat. Commun.*, 2020, **11**, 1391.
32 M. H. Park, D. H. Lee, K. Yang, J.-Y. Park, G. T. Yu, H. W. Park, M. Materano, T. Mittmann, P. D. Lomenzo, T. Mikolajick, U. Schroeder and C. S. Hwang, *J. Mater. Chem. C*, 2020, **8**, 10526–10550.
33 T. Song, S. Estandía, N. Dix, J. Gàzquez, M. Gich, I. Fina and F. Sánchez, *J. Mater. Chem. C*, 2022, **10**, 8407–8413.
34 Y. Wei, P. Nukala, M. Salverda, S. Matzen, H. J. Zhao, J. Momand, A. S. Everhardt, G. Agnus, G. R. Blake, P. Lecoeur, B. J. Kooi, J. Íñiguez, B. Dkhil and B. Noheda, *Nat. Mater.*, 2018, **17**, 1095.
35 J. P. B. Silva, R. F. Negrea, M. C. Istrate, S. Dutta, H. Aramberri, J. Iniguez, F. G. Figueiras, C. Ghica, K. C. Sekhar and A. L. Kholkin, *ACS Appl. Mater. Interfaces*, 2021, **13**, 51383.
36 A. El Boutaybi, T. Maroutian, L. Largeau, S. Matzen and P. Lecoeur, *Phys. Rev. Mater.*, 2022, **6**, 074406.
37 M. Zheng, Z. Yin, Y. Cheng, X. Zhang, J. Wu and J. Qi, *Appl. Phys. Lett.*, 2021, **119**, 172904.
38 Y. Yun, P. Buragohain, M. Li, Z. Ahmadi, Y. Zhang, X. Li, H. Wang, J. Li, P. Lu, L. Tao, H. Wang, J. E. Shield, E. Y. Tsymbal, A. Gruverman and X. Xu, *Nat. Mater.*, 2022, **21**, 903.
39 S. V. Barabash, *J. Comput. Electron.*, 2017, **16**, 1227–1235.
40 T. D. Huan, V. Sharma, G. A. Rossetti and R. Ramprasad, *Phys. Rev. B: Condens. Matter Mater. Phys.*, 2014, **90**, 064111.
41 Y. Qi, S. Singh, C. Lau, F.-T. Huang, X. Xu, F. J. Walker, C. H. Ahn, S.-W. Cheong and K. M. Rabe, *Phys. Rev. Lett.*, 2020, **125**, 257603.
42 L. Azevedo Antunes, R. Ganser, C. Kuenneth and A. Kersch, *Phys. Status Solidi RRL*, 2022, **16**, 2100636.
43 J. Müller, T. S. Böscke, U. Schröder, S. Mueller, D. Bräuhaus, U. Böttger, L. Frey and T. Mikolajick, *Nano Lett.*, 2012, **12**, 4318–4323.
44 M. H. Park, Y. H. Lee, H. J. Kim, Y. J. Kim, T. Moon, K. D. Kim, J. Müller, A. Kersch, U. Schroeder, T. Mikolajick and C. S. Hwang, *Adv. Mater.*, 2015, **27**, 1811–1831.
45 Z. Wang, A. A. Gaskell, M. Dopita, D. Kriegner, N. Tasneem, J. Mack, N. Mukherjee, Z. Karim and A. I. Khan, *Appl. Phys. Lett.*, 2018, **112**, 222902.
46 B. Xu, P. D. Lomenzo, A. Kersch, T. Mikolajick and U. Schroeder, *ACS Appl. Electron. Mater.*, 2022, **4**, 3648–3654.
47 J. Adam and M. D. Rogers, *Acta Crystallogr.*, 1959, **12**, 951.
48 R. Ruh and P. W. R. Corfield, *J. Am. Ceram. Soc.*, 1970, **53**, 126–129.
49 E. H. Kisi and C. J. Howard, *Key Eng. Mater.*, 1998, **154**, 1.
50 H. Arashi, *J. Am. Ceram. Soc.*, 1992, **75**, 844–847.
51 O. Ohtaka, H. Fukui, T. Kunisada, T. Fujisawa, K. Funakoshi, W. Utsumi, T. Irifune, K. Kuroda and T. Kikegawa, *Phys. Rev. B: Condens. Matter Mater. Phys.*, 2001, **63**, 174108.
52 C. J. Howard, E. H. Kisi and O. Ohtaka, *J. Am. Ceram. Soc.*, 1991, **74**, 2321–2323.
53 A. Kersch, R. Ganser and M. Trien, *Front. Nanotechnol.*, 2022, **4**, 2673–3013.
54 M. Materano, P. Reinig, A. Kersch, M. Popov, M. Deluca, T. Mikolajick, U. Boettger and U. Schroeder, *Phys. Status Solidi RRL*, 2022, **16**, 2100589.
55 S. Fan, S. Singh, X. Xu, K. Park, Y. Qi, S. W. Cheong, D. Vanderbilt, K. M. Rabe and J. L. Musfeldt, *npj Quantum Mater.*, 2022, **7**, 32.
56 A. Raeliarijaona and R. E. Cohen, *Appl. Phys. Lett.*, 2022, **120**, 0003–6951.
57 R. Dovesi, A. Erba, R. Orlando, C. M. Zicovich-Wilson, B. Civalleri, L. Maschio, M. Rérat, S. Casassa, J. Baima, S. Salustro and B. Kirtman, *Wiley Interdiscip. Rev.: Comput. Mol. Sci.*, 2018, **8**, e1360.
58 D. Vilela Oliveira, J. Laun, M. F. Peintinger and T. Bredow, *J. Comput. Chem.*, 2019, **40**, 2364–2376.
59 L. Valenzano, B. Civalleri, S. Chavan, S. Bordiga, M. H. Nilsen, S. Jakobsen, K. P. Lillerud and C. Lamberti, *Chem. Mater.*, 2011, **23**, 1700.
60 T. Bredow and M. Lerch, *Zeitschrift für anorganische und allgemeine Chemie*, 2004, **630**, 2262–2266.
61 A. D. Becke, *J. Chem. Phys.*, 1993, **98**, 5648.
62 C. Lee, W. Yang and R. G. Parr, *Phys. Rev. B: Condens. Matter Mater. Phys.*, 1988, **37**, 785.
63 R. Demichelis, B. Civalleri, M. Ferrabone and R. Dovesi, *Int. J. Quantum Chem.*, 2010, **110**, 406–415.
64 H. J. Monkhorst and J. D. Pack, *Phys. Rev. B: Condens. Matter Mater. Phys.*, 1976, **13**, 5188–5192.
65 C. Pisani, R. Dovesi, C. Roetti, M. Causà, R. Orlando, S. Casassa and V. R. Saunders, *Int. J. Quantum Chem.*, 2000, **77**, 1032–1048.
66 R. Demichelis, H. Suto, Y. Noël, H. Sogawa, T. Naoi, C. Koike, H. Chihara, N. Shimobayashi, M. Ferrabone and R. Dovesi, *Mon. Not. R. Astron. Soc.*, 2012, **420**, 147–154.
67 L. Maschio, B. Kirtman, R. Orlando and M. Rèrat, *J. Chem. Phys.*, 2012, **137**, 204113.
68 F. Pascale, C. M. Zicovich-Wilson, F. López Gejo, B. Civalleri, R. Orlando and R. Dovesi, *J. Comput. Chem.*, 2004, **25**, 888.
69 A. Boileau, M. Dallocchio, F. Baudouin, A. David, U. Lüders, B. Mercey, A. Pautrat, V. Demange, M. Guilloux-Viry, W. Prellier and A. Fouchet, *ACS Appl. Mater. Interfaces*, 2019, **11**, 37302–37312.
70 H. Zhong, M. Li, Q. Zhang, L. Yang, R. He, F. Liu, Z. Liu, G. Li, Q. Sun, D. Xie, F. Meng, Q. Li, M. He, E.-J. Guo, C. Wang, Z. Zhong, X. Wang, L. Gu, G. Yang, K. Jin, P. Gao and C. Ge, *Adv. Mater.*, 2022, **34**, 2109889.
71 P. Roy, M. Rouzières, Z. Qi and O. Chubar, *Infrared Phys. Technol.*, 2006, **49**, 139–146.
72 R. C. Garvie, *J. Phys. Chem.*, 1965, **69**, 1238–1243.
73 E. Bonera, G. Scarel and M. Fanciulli, *J. Non-Cryst. Solids*, 2003, **322**, 105–110.
74 M. Hyuk Park, H. Joon Kim, Y. Jin Kim, T. Moon and C. Seong Hwang, *Appl. Phys. Lett.*, 2014, **104**, 072901.
75 T. Shiraishi, K. Katayama, T. Yokouchi, T. Shimizu, T. Oikawa, O. Sakata, H. Uchida, Y. Imai, T. Kiguchi, T. J. Konno and H. Funakubo, *Appl. Phys. Lett.*, 2016, **108**, 262904.

76 S. J. Lee, M. J. Kim, T. Y. Lee, T. I. Lee, J. H. Bong, S. W. Shin, S. H. Kim, W. S. Hwang and B. J. Cho, *AIP Adv.*, 2019, **9**, 125020.
77 T. Song, H. Tan, N. Dix, R. Moalla, J. Lyu, G. Saint-Girons, R. Bachelet, F. Sánchez and I. Fina, *ACS Appl. Electron. Mater.*, 2021, **3**, 2106–2113.
78 P. Nukala, M. Ahmadi, Y. Wei, S. de Graaf, E. Stylianidis, T. Chakrabortty, S. Matzen, H. W. Zandbergen, A. Björling, D. Mannix, D. Carbone, B. Kooi and B. Noheda, *Science*, 2021, **372**, 630–635.
79 S. E. Reyes-Lillo, K. F. Garrity and K. M. Rabe, *Phys. Rev. B: Condens. Matter Mater. Phys.*, 2014, **90**, 140103.
80 U. Vijayalakshmi, M. Chellappa, U. Anjaneyulu, G. Manivasagam and S. Sethu, *Mater. Manuf. Processes*, 2016, **31**, 95–106.
81 M. L. de Peres, R. de Avila Delucis, S. C. Amico and D. A. Gatto, *Nanomater. Nanotechnol.*, 2019, **9**, 1847980419876201.
82 A. Raeliarijaona and R. E. Cohen, *arXiv*, 2023, preprint, arXiv:2305.19446, DOI: **10.48550/arXiv.2305.19446**.
83 L. Eyring and B. O. Holmberg, *Nonstoichiometric Compounds*, American Chemical Society, 1963, vol. 39, pp. 4–46.
84 G.-y Adachi and N. Imanaka, *Chem. Rev.*, 1998, **98**, 1479–1514.
85 Z. Kang and L. Eyring, *J. Alloys Compd.*, 1997, **249**, 206–212.
86 H. Hasegawa, *J. Mater. Sci. Lett.*, 1983, **2**, 91–93.
87 H. Hasegawa, T. Hioki and O. Kamigaito, *J. Mater. Sci. Lett.*, 1985, **4**, 1092–1094.
88 G. Sattonnay and L. Thomé, *J. Nucl. Mater.*, 2006, **348**, 223–227.
89 D. P. Burke and W. M. Rainforth, *J. Mater. Sci. Lett.*, 1997, **16**, 883–885.
90 H.-K. Kim, K.-W. Yoo, S.-J. Kim and C.-H. Jung, *Materials*, 2021, **14**, 5321.
91 Y. Maruo, K. Yoshihara, M. Irie, G. Nishigawa, N. Nagaoka, T. Matsumoto and S. Minagi, *J. Appl. Biomater. Biomech.*, 2020, **18**, 2280800020942717.
92 V. Lenzi, J. P. B. Silva, B. Šmíd, V. Matolín, C. M. Istrate, C. Ghica, J. L. MacManus-Driscoll and L. Marques, *Energy Environ. Mater.*, 2022, e12500.